ACS Sustainable Chemistry & Engineering

pubs.acs.org/journal/ascecg

Research Article

Effect of Impurities on the Decarbonization of Calcium Carbonate Using Aqueous Sodium Hydroxide

Marco Simoni,* Theodore Hanein,* Chun Long Woo, John Provis, and Hajime Kinoshita*

Cite This: *ACS Sustainable Chem. Eng.* 2022, 10, 11913−11925

Read Online

ACCESS | Metrics & More | Article Recommendations | Supporting Information

ABSTRACT: Decarbonizing calcium carbonate ($CaCO_3$) is a crucial step for a wide range of major industrial processes and materials, including Portland cement (PC) production. Apart from the carbon footprint linked to fuel combustion, the process CO_2 embodied within $CaCO_3$ represents the main concern for the sustainability of production. Our recent works demonstrated that it is possible to avoid both the fuel and process CO_2 by reacting $CaCO_3$ with aqueous NaOH and obtain $Ca(OH)_2$ and $Na_2CO_3{\cdot}xH_2O$ (x = 0 and 1). This present study provides a further understanding of the process by testing different raw calcareous sources. A high decarbonization (~80%) of $CaCO_3$ was achieved for silica-rich chalk, whereas a lower extent was obtained (~50%) for limestone. To understand the difference in their reaction behavior, the effect of impurities was studied. The effects of the major impurities (Si, Al, and Fe) were found to be marginal, which is advantageous to process industrial grade materials, while the morphology of the raw materials presents a significant impact. The applicability of our decarbonization technology was also demonstrated on magnesite ($MgCO_3$).

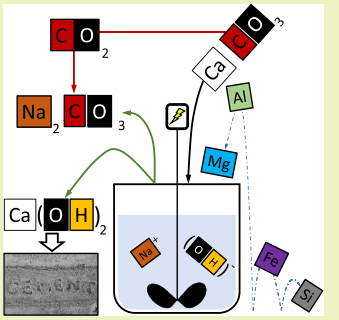

KEYWORDS: *decarbonization, CO_2 sequestration, ambient conditions, cement, $CaCO_3$*

1. INTRODUCTION

The calcination of calcium carbonate to obtain lime ($CaCO_3 \rightarrow CaO + CO_2$) is currently considered one of the major contributors to the global CO_2 emissions due to both the large global demand[1] and the specific carbon footprint (1.0−1.8 kg_{CO2}/kg_{CaO}).[2] The Portland cement (PC) industry is currently utilizing the largest portion of calcined limestone, with a global market size of 4 Gt PC per year,[3] which makes the cement industry responsible for about 8% of the total CO_2 emissions worldwide[4] and 12−15% of global industry energy use.[5]

The calcination of calcium carbonate usually involves two distinct emission sources: process- and fuel-derived CO_2. The former arises from the calcination stoichiometry (0.44 kg_{CO2}/kg_{CaCO3}),[6] while the latter is linked to the combustion of the hydrocarbon fuels to attain the required pyro-processing temperatures (~900 °C[2,7] for lime production and 1500 °C[5] for PC production). Although the fuels represent the largest portion of the overall economic operating costs for both lime and cement industries,[8] the process CO_2 represents the biggest challenge for their sustainable production. The process CO_2 accounts for the majority of the CO_2 emissions from the limestone calcination step, and several solutions have been proposed: Carbon Capture & Storage (CCS) technologies,[9] the switch to sustainable fuels,[7,10] and the development of low-calcium cements.[11] Currently, the CCS technologies are believed to have the highest potential to decarbonize the cement industry. They might be classified as pre- or post-combustion; while the former options require a deep modification of the current design, the latter ones are usually retrofittable with the conventional lime and cement plants.[12−14] Among the CCS technologies available, the CO_2 removal through reaction with monoethanolamine (MEA) solutions appears to be the most developed solution so far,[9] despite the high operational costs linked to the regeneration of the solvent.[15] The use of waste as fuel is a common practice already, accounting for a significant replacement of fossil sources in the EU depending on the country;[16] the selection and pretreatment of the waste are essential to ensure a good quality of the manufactured product. The use of alternative binders with a lower Ca content would reflect a production with limited process CO_2 emissions. In addition, the reuse of several types of waste as substitutes to the conventional cement chemistry might play a determining role in the waste disposal challenge.[17] These potential solutions are all based on the high-temperature calcination process.

In contrast, we recently proposed an alternative technology that exploits the chemical interaction between $CaCO_3$ and NaOH in an aqueous system under ambient conditions[18] so that the high-temperature calcination process itself can be avoided. On the other hand, the application of such a

Received: May 18, 2022
Revised: August 16, 2022
Published: August 26, 2022

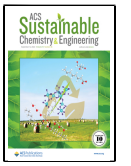

decarbonization route would require a drastic modification of the current plants, with high investment costs associated. Moreover, the significant usage of NaOH would raise concerns in terms of embodied CO_2 and Cl_2 emissions from the chlor-alkali process.[19] Despite this, since the chlor-alkali process is mainly sustained by electric energy,[19] the NaOH production would be expected to be carbon-neutral by 2050 if the goals set up during the Paris agreement in 2015 will be met.[20] Regarding Cl_2, its disposal might partially be performed through recycling into Cl-based cements, such as alinite.[21,22] As shown in eq 1, the alternative decarbonization route leads to the synthesis of $Ca(OH)_2$, which can also be converted to CaO in mild conditions through dehydroxylation, $Ca(OH)_2 \rightarrow CaO + H_2O$,[7] while sequestrating the process CO_2 into a stable mineral form, i.e., $Na_2CO_3{\cdot}xH_2O$ (x = 0 and 1).

$$CaCO_3 + 2NaOH + xH_2O \rightarrow Ca(OH)_2 + Na_2CO_3{\cdot}xH_2O\ (x = 0 \text{ and } 1) \quad (1)$$

For cement clinker production, high temperatures are still required for the formation of clinker phases,[1] but such conditions can be achieved through electrical heating[5] and E-fuels,[23] concentrated solar power,[24] or combustion of waste/biomass.[25]

Our previous work[18] demonstrated the feasibility of the proposed decarbonization technique on reagent grade calcium carbonate and a particular calcium carbonate (chalk) source. For the industrial applications, variabilities in the raw material source are inevitable, which would affect the process.[1,26] In the present study, two different industrial grade materials with significantly different compositions, a limestone and a chalk (same as in our previous work[18]), are considered.

Limestone and chalk are mainly calcium carbonate but are generally different both at macro- and microscopic levels,[27] and this allows us to assess the efficiency of our process for varying calcareous sources. Due to the nature of our aqueous process, it is envisaged that the different average porosities (chalk, >25%;[28] limestone, <10%[29]) will play a crucial role in the present investigation. A higher or lower permeability and diffusion of foreign elements (e.g., Na^+) could make the difference between more and less reactive materials for the scope of this technology; generally, the higher the porosity (ϕ), the higher the permeability (k).[30]

In this work, deeper insight into the mechanisms ruling the reaction is discussed by considering different calcareous sources with varying contents of impurities. The different efficiencies registered could suggest an important effect of varying contents of impurities (Si, Al, Fe, and Mg) in the reactants. For this reason, the effect of each of them was isolated in reagent grade binary systems with increasing $CaCO_3$ content, and the outcomes are thoroughly discussed and justified by cross-linking analyses. Finally, to detect those parameters, i.e., impurity content or particle morphology, which could mostly influence the reaction efficiency, reagent grade systems simulating the compositions of the chalk and limestone were tested. The authors are well aware that additional considerations must be done in terms of process design (including the hazards linked to the high concentration of the NaOH solutions used), energy consumption, and carbon balance before even considering a process scale-up; despite this, the outcomes reported here would still provide a valid baseline for further considerations to be done.

2. EXPERIMENTAL SECTION

2.1. Materials. The present work used the following commercial grade chemicals: Sigma-Aldrich $CaCO_3$ (≥99%), Honeywell Fluka NaOH (≥97%), Sigma-Aldrich purum p.a. white quartz as a SiO_2 source (≥95%), Acros Organics extra pure Al_2O_3 (99%), Fisher Chemical pure Fe_2O_3 (99.85%), and Honeywell $MgCO_3$ basic (MgO > 40%). Their solubilities in water and methanol are reported in Table S1. The industrial grade limestone and chalk used in the present work were provided by CEMEX; their oxide compositions (Table 1) were obtained via X-ray fluorescence (XRF).

Table 1. Oxide Composition (wt %) of the Limestone and Chalk Used, Together with the Respective Loss on Ignition (LOI) Values Gained by XRF

	$CaCO_3$	SiO_2	Al_2O_3	Fe_2O_3	$MgCO_3$	others (K, Ti, P)	LOI (%)
limestone	94.4	1.2	0.3	0.5	3.2	<1.0	42.3
chalk	74.2	19.9	2.8	1.0	0.7	<1.5	29.4

Considering the loss on ignition values of 29.4% for the chalk and 42.3% for the limestone, the Ca and Mg content is reported as $CaCO_3$ and $MgCO_3$ rather than CaO and MgO, respectively. The limestone presented a higher $CaCO_3$ content (94.4 wt %) with respect to the chalk (74.2 wt %). A significant silica content (19.9 wt %) was detected within the chalk, whereas more $MgCO_3$ (3.2 wt %) were found in the limestone. Traces of Fe_2O_3 were also detected in both materials. To compare the results between the reagent and industrial grade calcareous sources, the raw materials were manually sieved below 38 μm. As reported in Figure S1, the PSD analysis revealed average diameters (Dx50) of 6.0 and 8.5 μm for the chalk and limestone, respectively; most of the reagent grade $CaCO_3$ solid particles were in the range of 20−40 μm, with a negligible amount of smaller (5 μm) ones.

2.2. Characterization Techniques. *2.2.1. X-ray Diffraction (XRD).* X-ray diffraction (XRD) was used to identify the reaction products. The measurements were performed using a Bruker D2 PHASER desktop X-ray diffractometer in Bragg−Brentano geometry, with a Cu-Kα radiation source running at 30 kV and 10 mA, a one-dimensional LYNXEYE detector, and a 1 mm divergence slit. Powdered samples were loaded onto 2.5 cm-diameter and 1 mm-deep sample holders. Each pattern was recorded between 5° and 80° 2θ, with a step size of 0.02° at 0.5 s per step, with the stage rotating at 15 rpm. Qualitative phase identification was carried out using the Highscore-Plus software and PDF-42019 database.

2.2.2. Thermogravimetry (TG/DTG). Thermogravimetric analysis (TG) was carried out on the reaction products. Approximately 40 mg of sample was analyzed on a PerkinElmer TG 4000 from 30 to 800 °C at a heating rate of 10 °C/min with a 40 mL/min N_2 flow. The sample was then held at 800 °C for 1 h to ensure complete loss of CO_2 from $CaCO_3$ while maintaining Na_2CO_3 without melting or decomposing. To identify evolving gases, a Hiden mass spectrometer (HPR-20 GIC EGA) was used to record the signals for H_2O and CO_2. As shown in eq 2, the extent of reaction α was calculated from the weight losses in the temperature ranges corresponding to the thermal decomposition of $Ca(OH)_2$ (310−470 °C[31]) and $CaCO_3$ (560−800 °C[32]). The terms $w\%_{[phase]}$ and MW_{phase} refer to the weight loss registered in TG and the molecular weight of the substance considered, respectively. The content of $Na_2CO_3{\cdot}H_2O$ could similarly be estimated from mass loss in the temperature range of 50−130 °C.[33] The possible measurement error was estimated by analyzing the same sample six times under the same condition as ±0.16 wt % for $Na_2CO_3{\cdot}H_2O$, ±0.10 wt % for $Ca(OH)_2$, and ±0.16 wt % for $CaCO_3$.

https://doi.org/10.1021/acssuschemeng.2c02913
ACS Sustainable Chem. Eng. 2022, 10, 11913−11925

Table 2. Compositions Inspected for the Limestone (L Series) and Chalk (C Series) and the Corresponding NaOH/$CaCO_3$ (mol/mol) and H_2O/Solids (w/w) Ratios

sample ID	H_2O (wt %)	NaOH (wt %)	feed material (wt %)	NaOH/$CaCO_3$ (mol/mol)	H_2O/feed material (w/w)	NaOH (mol· kg_{H2O}^{-1})
L_w/s_0.7	24.8	40.3	35.0	3.0	0.7	40.6
L_w/s_1.0	31.8	36.4	31.7	3.0	1.0	28.6
L_w/s_1.5	41.2	31.4	27.4	3.0	1.5	19.0
L_w/s_2.0	48.2	27.7	24.1	3.0	2.0	14.3
L_w/s_3.0	58.2	22.4	19.4	3.0	3.0	9.6
L_w/s_5.0	69.9	16.1	14.0	3.0	5.0	5.7
C_w/s_0.6	24.4	35.1	40.5	3.0	0.6	36.0
C_w/s_0.7	27.4	34.0	38.7	3.0	0.7	31.1
C_w/s_1.0	34.8	30.4	34.8	3.0	1.0	21.8
C_w/s_1.5	44.5	25.8	29.6	3.0	1.5	14.5
C_w/s_2.0	51.7	22.5	25.8	3.0	2.0	10.9
C_w/s_3.0	61.6	18.0	20.4	3.0	3.0	7.3
C_w/s_5.0	72.7	12.7	14.5	3.0	5.0	4.4

Table 3. Composition of Starting Solid Mixtures (wt %) of the Binary Systems and NaOH/$CaCO_3$ (mol/mol) and H_2O/Solids (w/w) Ratios Used in the Reactions

sample ID	$\nu CaCO_3$ (wt %)	νSiO_2 (wt %)	νAl_2O_3 (wt %)	νFe_2O_3 (wt %)	$\nu MgCO_3$ (wt %)	NaOH/$CaCO_3$ (mol/mol)	H_2O/solids (w/w)
reference	100.0	0.0				3.9	4.0
SiO_2_1.0%	99.0	1.0				4.0	4.0
SiO_2_2.9%	97.1	2.9				4.0	3.9
SiO_2_4.8%	95.2	4.8				4.0	3.8
SiO_2_6.5%	93.5	6.5				4.0	3.7
SiO_2_9.1%	90.9	9.1				4.1	3.6
SiO_2_13.1%	86.9	13.1				4.0	3.5
SiO_2_20.0%	80.0	20.0				4.0	3.2
Al_2O_3_1.0%	99.0		1.0			4.0	4.0
Al_2O_3_2.0%	98.0		2.0			4.0	3.9
Al_2O_3_2.9%	97.1		2.9			4.0	3.9
Al_2O_3_4.8%	95.2		4.8			4.0	3.8
Fe_2O_3_0.5%	99.5			0.5		4.0	4.0
Fe_2O_3_1.0%	99.0			1.0		4.0	4.0
Fe_2O_3_1.5%	98.5			1.5		4.0	3.9
Fe_2O_3_2.0%	98.0			2.0		4.0	3.9
Fe_2O_3_4.8%	95.2			4.8		4.0	3.8
Fe_2O_3_9.1%	90.9			9.1		4.0	3.6
$MgCO_3$_0.6%	99.4				0.6	4.0	4.0
$MgCO_3$_1.0%	99.0				1.0	4.0	3.9
$MgCO_3$_1.5%	98.5				1.5	4.0	4.0
$MgCO_3$_4.8%	95.2				4.8	4.0	3.8
$MgCO_3$_9.1%	90.9				9.1	4.0	3.6
$MgCO_3$_16.7%	83.3				16.7	4.0	3.3

$$\alpha = \frac{w\%_{[Ca(OH)_2]}}{MW_{Ca(OH)_2}} \Big/ \left[\frac{w\%_{[Ca(OH)_2]}}{MW_{Ca(OH)_2}} + \frac{w\%_{[CaCO_3]}}{MW_{CaCO_3}} \right] \quad (2)$$

2.2.3. Scanning Electron Microscopy (SEM). Scanning electron microscopy with energy-dispersive X-ray spectroscopy (SEM−EDX; Hitachi TM3030) was used for the microstructural analysis of the starting powders and reaction products at a 15 kV voltage and working distance of approximately 9 ± 0.2 mm. This was fitted with the Bruker Quantax Energy Dispersive X-ray Spectrometer for compositional analysis through BSE detectors. The reaction products were mounted, in powder form, in epoxy resin without crushing and left to harden for 72 h. The analysis surface was ground manually with progressively finer abrasives, up to a 1 μm finish,[34] and further polished by using diamond pastes of 6, 3, 2, 1, and 0.25 μm (MetPrep). The samples then underwent a three-step carbon coating and were back-loaded to a metallic holder. Electrically conductive silver paint (RS Components) was applied at the interface between the metallic base epoxy resin to ensure the sufficient conductivity and, therefore, good quality of the SEM micrographs.

2.2.4. X-ray Fluorescence (XRF). X-ray fluorescence was used to quantify the elemental composition of the unreacted and reacted solids; the measurement was performed through a PW4404 AMG Analytical spectrometer, with an Ar/CH_4 gas flow and a Rh X-ray tube. Samples were crushed and milled to obtain a particle size within the range of 100−250 μm. The milled materials were dried at 110 °C until a constant weight was achieved. The powder was mixed in the fusion vessel with a flux, lithium tetraborate ($Li_2B_4O_7$), at a 1:10 sample-to-flux weight ratio and then fired at 1270 ± 15 °C for 12 min upon swirling. The detection limit of the XRF analysis depends on both the sample preparation and the atomic number Z of the targeted elements. Generally, detection limits of 20−1000, 5−10, and 1−20 $\mu g \cdot g^{-1}$ are reported for low-, medium-, and high-Z elements, respectively.[35] For this reason, the detection of Mg may be affected by the instrumental error since it belongs to the second group in the periodic table (Z = 12).

https://doi.org/10.1021/acssuschemeng.2c02913
ACS Sustainable Chem. Eng. 2022, 10, 11913−11925

2.3. Reaction Procedure. Despite the specific conditions stated below for each targeted investigation, all the experiments were conducted according to the same experimental procedure. Upon dissolution of NaOH in water at known molalities (m), the solutions were left to cool down to room temperature. The solids were dried at 35 °C overnight prior reaction to remove the weakly bound water, which might slightly affect the overall NaOH concentration used. The reaction was carried out in a 250 mL PTFE beaker to avoid corrosion that may be caused by the hyper-alkaline NaOH solutions, and a stirring rate of 1050 rpm was ensured through a Heidolph R2020 overhead mixer equipped with a PTFE centrifugal stirrer shaft (40 mm diameter). The reaction was carried out under ambient/laboratory conditions ($T \approx 20$ °C) for a residence time of 300 s. To remove the unreacted NaOH after reaction, all the samples discussed above were washed with methanol for further 300 s. Considering the solubility of NaOH in methanol at 20 °C (238 g/L[36]) and the amount of NaOH in the starting mixtures, the complete removal of NaOH was ensured by choosing a methanol-to-NaOH weight (g/g) ratio of 4. Given the negligible solubility of the targeted phases $Ca(OH)_2$,[37] $Na_2CO_3{\cdot}H_2O$,[38] Na_2CO_3,[38] $CaCO_3$,[39] SiO_2,[40] Al_2O_3,[41] Fe_2O_3,[41] and $MgCO_3$[41] in organic solvents, no variation of the solid mixture should have occurred upon washing with methanol. Finally, the reaction products obtained from all the experiments discussed in the present work were collected on a Whatman Grade 1 (90 mm) filter paper using vacuum-assisted Büchner funnel filtration, dried in an oven at 35 °C for 2 h, weighed, ground, and sieved below 63 μm for characterization.

2.3.1. Decarbonization of Industrial Grade Calcareous Materials. The industrial grade chalk and limestone were reacted with NaOH at the $NaOH/CaCO_3$ molar ratio of 3 based on the $CaCO_3$ contents obtained by XRF of the materials (Table 1). This ratio was previously found to positively influence the reaction yield.[18] The systems were tested at increasing water-to-solid weight ratio, which in return decreases the NaOH molalities in the aqueous solution (4 m−40 m). The detailed starting mix compositions are reported in Table 2.

2.3.2. Effect of Impurities (Si, Al, Fe, and Mg). The effect of common impurities in the chalk and limestone (i.e., Si, Al, Fe, and Mg) on the decarbonization reaction was studied. Binary systems of $CaCO_3$-SiO_2, $CaCO_3$-Al_2O_3, $CaCO_3$-Fe_2O_3, and $CaCO_3$-$MgCO_3$ were tested using reagent grade chemicals at varying proportions (Table 3) to simulate the oxide compositions of the chalk and limestone (Table 1). This would isolate the effect of each main impurity and allow for the assessment of their effects on the overall reaction.

Prior to the reaction, the minerals were ground, sieved below 38 μm, and dried at 35 °C overnight to ensure the homogeneous particle size and limited presence of water, which might lower the overall NaOH concentration used. The 10 m NaOH solutions were prepared to ensure a $NaOH/CaCO_3$ molar ratio of 4 for all the samples. Despite the decreasing w/s ratios used at higher additions of SiO_2, Al_2O_3, Fe_2O_3, and $MgCO_3$ (Table 3), previous investigations revealed that such a parameter would not affect the reaction efficiency in the ranges considered here. A high content of water was chosen for the starting mixture to avoid the agglomeration of solids and, therefore, error.

To study the effect of the coexisting impurities, reagent grade chemicals were also blended according to the proportions reported in Table 4, simulating the industrial grade chalk and limestone used in the present work (Table 1).

Table 4. $CaCO_3$, SiO_2, Al_2O_3, and $MgCO_3$ Contents for the Chalk_R.G. and Limestone_R.G. Powders Simulating the Industrial Grade Chalk and Limestone

sample ID	$\nu CaCO_3$ (wt %)	νSiO_2 (wt %)	νAl_2O_3 (wt %)	νFe_2O_3 (wt %)	$\nu MgCO_3$ (wt %)
Chalk_R.G.	75.2	20.2	2.8	1.1	0.7
Limestone_R.G.	94.9	1.2	0.3	0.4	3.2

These mixtures simulating chalk and limestone were tested in the same way as in the testing of the industrial grade materials (Section 2.3.1), including the starting mix composition (Table 5).

3. RESULTS AND DISCUSSION

3.1. Industrial Grade Calcareous Materials. The TG analysis (Figure 1) performed on the unreacted raw calcareous materials confirmed the XRF quantification of $CaCO_3$ reported in Table 1, with slight variations: $CaCO_3$ contents of 73.7 wt % (33.7% of weight loss) and 96.8 wt % (42.9% of weight loss) for the chalk and limestone, respectively.

The SEM analysis was used to assess the overall differences of the two materials tested. First, large particles of unreacted chalk and limestone were selected through manual sieving, mounted in epoxy resin, and analyzed (Figure 2A,B), revealing their morphological characteristics. At first sight, the chalk appeared more porous than the limestone, with a more irregular surface.

The SEM analysis was repeated on the smaller particles (below 38 μm), not epoxy-mounted, but attached to a conductive carbon adhesive tape. The conventional coccolith-like[42] shaped $CaCO_3$ crystals are observed for the chalk, visible as light gray circles in Figure 3A. In contrast, a heterogeneous morphology could be observed for the limestone, whose $CaCO_3$ crystals were showing larger beads of scalenohedral[43] and smaller beads of cubic[44] geometry (Figure 3B). For completion, the SEM analysis was performed on the reagent grade $CaCO_3$ used for comparison with industrial grade materials; as shown in Figure 3C, it was mainly composed of thin plates arranged in spherical agglomerations.

3.2. Decarbonization of Industrial Grade Calcareous Materials. The industrial grade limestone and chalk were reacted with NaOH solutions at a constant $NaOH/CaCO_3$ molar ratio of 3 with increasing water-to-feed material ratio, as reported in Table 2. As shown in the TG/DTG data in Figure 4A, the dehydroxylation of $Na_2CO_3{\cdot}H_2O$ and $Ca(OH)_2$ between 50 and 130 °C and between 310 and 470 °C, respectively, and the decarbonization of the remaining $CaCO_3$ between 560 and 800 °C could be detected for the chalk samples.

The comparison between the XRD patterns for the unreacted and reacted chalk reported in Figure 4B confirmed the outcomes from the TG analysis. Indeed, only $Na_2CO_3{\cdot}H_2O$, $Ca(OH)_2$, and $CaCO_3$ could be identified as reaction products. Given the relatively low content in impurities, their eventual dissolution could not be assessed through XRD analysis despite the fact that the decreasing intensity of the main peak linked to SiO_2 (26.6° 2θ) would suggest that the dissolution of silica would occur upon the reaction. To assess that, XRF analysis was conducted on the sample C_w/s_0.7, showing the highest capability to convert $CaCO_3$ to products. Given that the solids would undergo a weight increase upon decarbonization reaction,[45] the ratio between the weight percentage of Ca and the specific foreign element was taken as the mass balance for the system. These values are reported in Table 6, which show the mass balance performed prior to and upon the reaction. Apparently, all the foreign elements were dissolving at a certain extent upon the reaction, as outlined by the lower Si/Ca, Al/Ca, Fe/Ca, and Mg/Ca ratios with respect to the initial values. Silica was the main component in the chalk, after $CaCO_3$, and the SEM micrograph reported in Figure S2A shows an irregular geometry that might be the cause of the dissolution observed.

https://doi.org/10.1021/acssuschemeng.2c02913
ACS Sustainable Chem. Eng. 2022, 10, 11913−11925

Table 5. Summary of the Conditions Used for the Reaction of the Reagent Grade Powders Simulating the Industrial Grade Materials Tested and Discussed in Section 2.3.1

sample ID	H_2O (wt %)	NaOH (wt %)	solids (wt %)	NaOH/$CaCO_3$ (mol/mol)	H_2O/solids (w/w)	NaOH (mol/L)
L_R.G._w/s_0.7	24.8	40.3	34.9	3.0	0.7	40.6
L_R.G._w/s_1.0	31.9	36.5	31.7	3.0	1.0	28.6
L_R.G._w/s_1.5	41.2	31.4	27.4	3.0	1.5	19.0
L_R.G._w/s_2.0	48.2	27.7	24.1	3.0	2.0	14.4
L_R.G._w/s_3.0	58.2	22.4	19.4	3.0	3.0	9.6
L_R.G._w/s_5.0	69.9	16.1	14.0	3.0	5.0	5.7
C_R.G._w/s_0.6	24.4	35.2	40.4	3.0	0.6	36.0
C_R.G._w/s_0.7	27.3	34.0	38.7	3.0	0.7	31.1
C_R.G._w/s_1.0	34.8	30.4	34.8	3.0	1.0	21.8
C_R.G._w/s_1.5	44.5	25.8	29.7	3.0	1.5	14.5
C_R.G._w/s_2.0	51.7	22.5	25.8	3.0	2.0	10.9
C_R.G._w/s_3.0	61.6	18.0	20.5	3.0	3.0	7.3
C_R.G._w/s_5.0	72.7	12.7	14.5	3.0	5.0	4.4

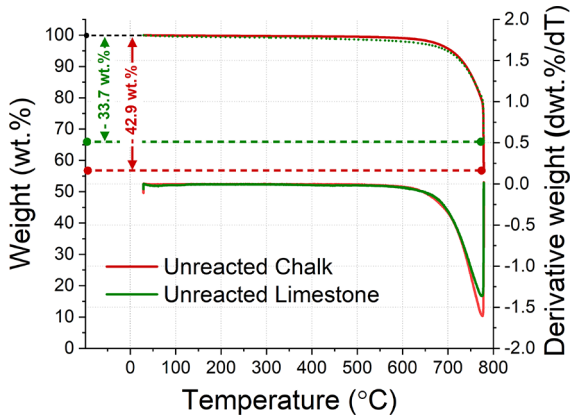

Figure 1. TG/DTG analysis performed for both the limestone and chalk studied.

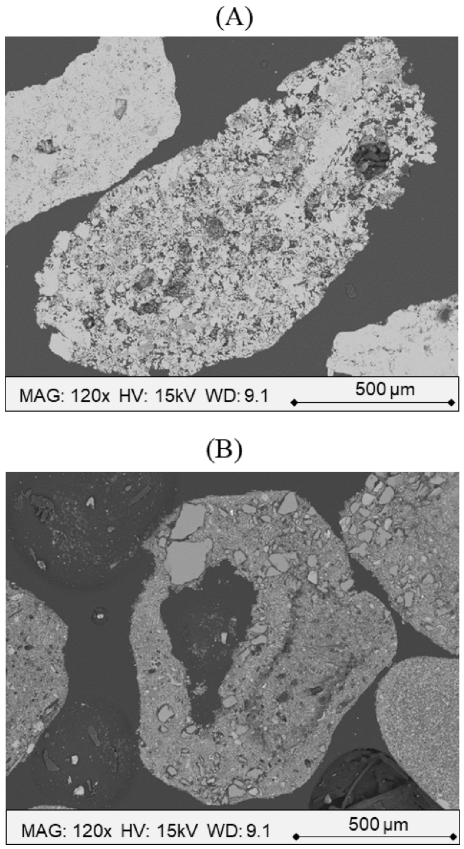

Figure 2. SEM micrographs of large-sized chalk (A) and limestone (B) unreacted particles at a magnification and working distance of 120× and 9.1 mm, respectively.

The TG analysis performed on the limestone (Figure 5A) revealed additional signals in the ranges of 140−200 and 250−350 °C for the samples reacted at higher w/s ratios; also, the sample L_w/s_3.0 showed an anomalous double peak in the region of 50−130 °C.

Given the higher $MgCO_3$ content within the limestone (Table 1), the signals between 250 and 350 °C were likely attributed to the dehydration of brucite $Mg(OH)_2$.[46] The signals between 140 and 200 °C may be linked to the dehydration of monohydrocalcite $CaCO_3 \cdot H_2O$,[47] suggesting its formation at generally higher water proportions. The double peak in the temperature region of 50−130 °C, with maxima at 85 and 102 °C, might potentially be due to the two-step dehydration of $Na_2CO_3 \cdot H_2O$,[48] which could not be observed for any other samples discussed here. The comparison between the XRD patterns of unreacted limestone and the sample L_w/s_3.0 (Figure 5B) supported the TG analysis. Slight traces of dolomite $CaMg(CO_3)_2$ could be observed for the limestone both prior to and upon the reaction, in accordance with the higher Mg content within the powders identified by XRF (Table 1). A similar intensity of the peaks of $CaCO_3$ suggests the limited reaction of $CaCO_3$ to form $Ca(OH)_2$, and weak intensities of brucite could also be observed. Again, the eventual dissolution of the foreign elements could be investigated by exploiting the XRF analysis performed on the sample showing the highest conversion extent (L_w/s_2.0). In contrast with the products from the reacted chalk, the Si/Ca, Al/Ca, Mg/Ca, and Fe/Ca ratios were decreasing for the sample L_w/s_2.0 upon the reaction (Table 6). Such an unexpected outcome would suggest that a portion of the calcium initially introduced would dissolve upon the reaction. Likely, the dissolution of dolomite to form brucite (Figure 5B) would contribute to the decreasing final Ca content within the solids. Potentially, given the relatively low content in Mg (Table 1), and therefore, dolomite, some of the calcite in the limestone would dissolve too. However, such a fact did not allow us to assess the eventual dissolution of the foreign elements Si, Al, Mg, and Fe for the limestone.

https://doi.org/10.1021/acssuschemeng.2c02913
ACS Sustainable Chem. Eng. 2022, 10, 11913−11925

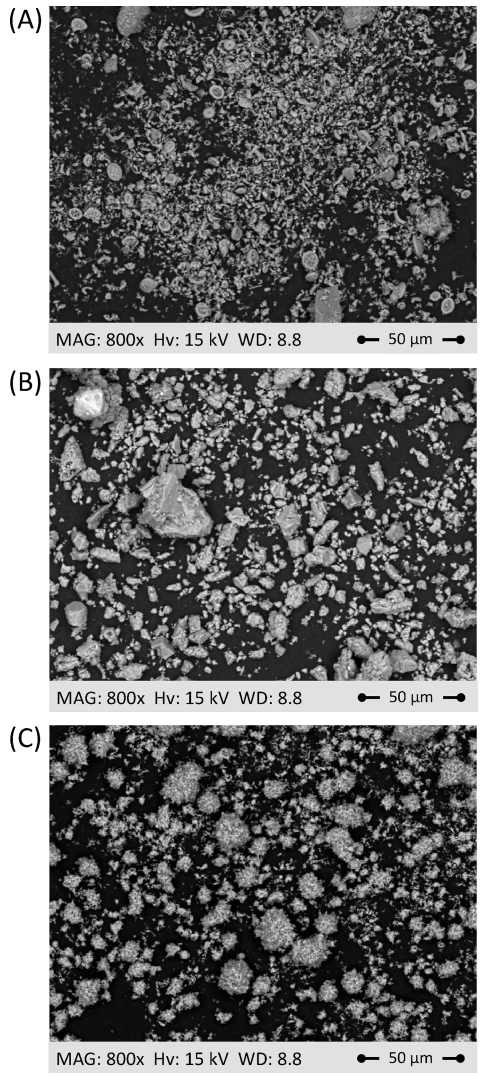

Figure 3. SEM micrographs of chalk (A), limestone (B), and reagent grade $CaCO_3$ (C) unreacted particles sieved below 38 μm at a magnification and working distance of 800× and 8.8, respectively.

Based on the amount of $Ca(OH)_2$ and $CaCO_3$ estimated through the TG data, the extent of the decarbonization reaction was assessed using eq 2. The outcomes of the assessment are plotted against the concentration of NaOH in Figure 6.

Since all samples have a constant NaOH/$CaCO_3$ ratio, the concentration of NaOH also represents the amount of H_2O in the system: the higher the NaOH concentration, the less the amount of H_2O. Despite the higher purity, the chalk appears to be much more reactive than the limestone, resulting in the higher extent of decarbonization (Figure 6). All materials, including the reagent grade $CaCO_3$, were showing a bell-shaped trend: the chalk indicated the maximum extent of decarbonization of 0.79 ± 0.02 at a NaOH concentration of 31.1 m, while the limestone achieved the maximum extent of decarbonization of 0.49 ± 0.02 at a NaOH concentration of 14.3 m. The reagent grade $CaCO_3$ showed the same trend observed for the other materials, registering the maximum extent of decarbonization of 0.86 ± 0.03 at a 20 m NaOH concentration.

3.3. Effect of Impurities: Individual Effect. The effects of major impurities were studied on the decarbonization

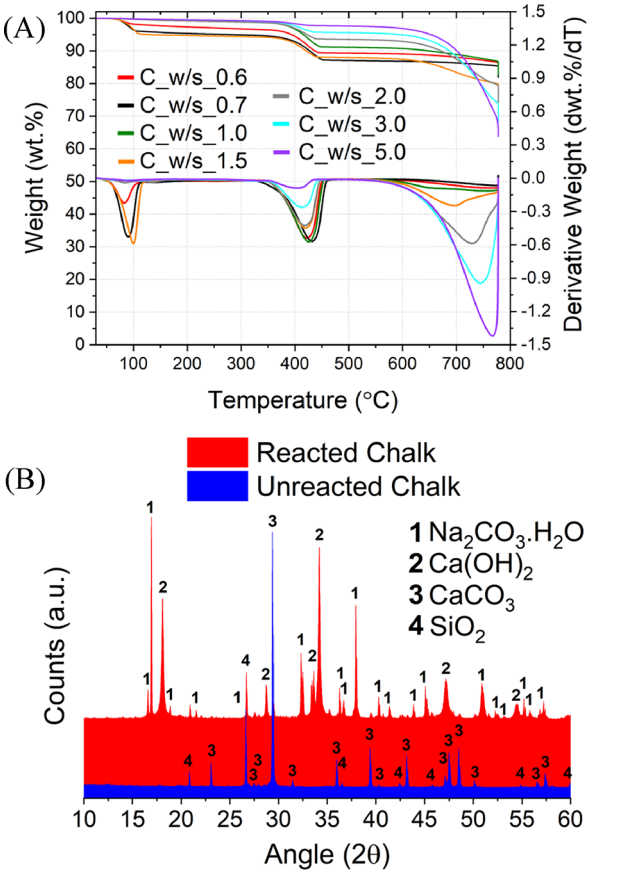

Figure 4. TG and DTG trends observed for all the chalk samples (A), together with the XRD patterns for C_w/s_0.7 and unreacted chalk powders (B).

reaction of the industrial grade materials. To isolate the effect of any individual impurity, reagent grade materials were used to test binary systems of $CaCO_3$-SiO_2, $CaCO_3$-Al_2O_3, $CaCO_3$-Fe_2O_3, and $CaCO_3$-$MgCO_3$, with varying proportions of impurities (Table 3). It is worth highlighting that the oxides of the targeted element were used here, rather than the corresponding minerals, such as corundum, hematite, and dolomite. For all systems, solid reaction products were recovered and underwent TG and XRD analysis. The quantification of the foreign elements was performed through XRF for those specimens showing the highest and lowest decarbonization efficiencies in each series. Representative XRD data for the solid reaction products of each system are shown in Figure 7. The XRD analysis confirms the occurrence of the decarbonization reaction with clear reflection peaks of $Ca(OH)_2$ and $Na_2CO_3{\cdot}H_2O$.

The TG analysis confirmed the presence of the main phases $Na_2CO_3{\cdot}H_2O$, $Ca(OH)_2$, and $CaCO_3$, with no additional signals detected for the SiO_2_n%, Al_2O_3_n%, and Fe_2O_3_n% series, as reported in Figure S3. Together with the XRD data just discussed (Figure 7), the absence of secondary reactions for these systems was confirmed except brucite formation in the CaO-$MgCO_3$ system. Differently, the weight losses observed between 250 and 350 °C for the $MgCO_3$_n% series (Figure 8) could likely be referring to the dehydration of brucite, as also confirmed by the XRD pattern of the sample $MgCO_3$_16.7% in Figure 7. Accordingly, the intensity of the signal was increasing at higher $MgCO_3$ proportions initially blended with $CaCO_3$.

https://doi.org/10.1021/acssuschemeng.2c02913
ACS Sustainable Chem. Eng. 2022, 10, 11913−11925

Table 6. Mass Balance for Each Element Prior to and upon the Reaction, Expressed as Si/Ca, Al/Ca, Fe/Ca, and Mg/Ca Ratios

	initial				final			
	Si/Ca	Al/Ca	Fe/Ca	Mg/Ca	Si/Ca	Al/Ca	Fe/Ca	Mg/Ca
C_w/s_0.7	3.1×10^{-01}	5.0×10^{-02}	2.4×10^{-02}	6.9×10^{-03}	1.4×10^{-01}	3.6×10^{-02}	1.8×10^{-02}	5.4×10^{-03}
L/w/s_2.0	1.5×10^{-02}	4.2×10^{-03}	7.5×10^{-03}	2.5×10^{-02}	3.2×10^{-02}	9.9×10^{-03}	1.3×10^{-02}	3.4×10^{-02}

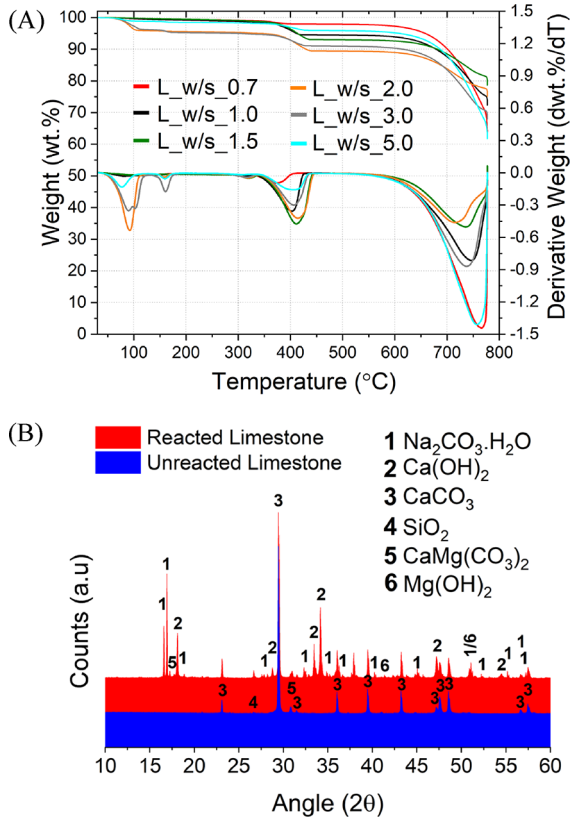

Figure 5. TG and DTG trends observed for all the limestone samples (A), together with the XRD patterns for L_w/s_3.0 and unreacted limestone powders (B).

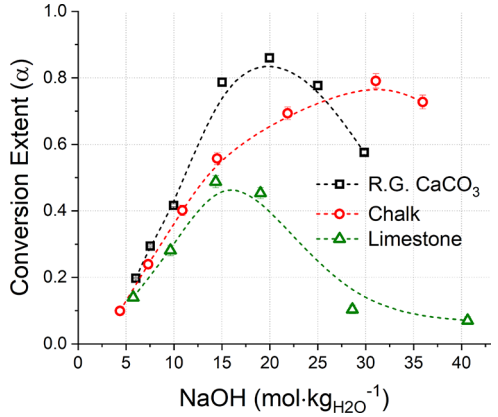

Figure 6. Overall efficiency of the systems at increasing NaOH molalities for the reacted chalk, limestone, and reagent grade $CaCO_3$, calculated by substituting the TG data into eq 2.

The quantification of $Na_2CO_3{\cdot}H_2O$, $Ca(OH)_2$, and $CaCO_3$, based on the TG data, allowed us to estimate the compositions of Na and Ca in the solid reaction product using eqs 3 and 4, respectively.

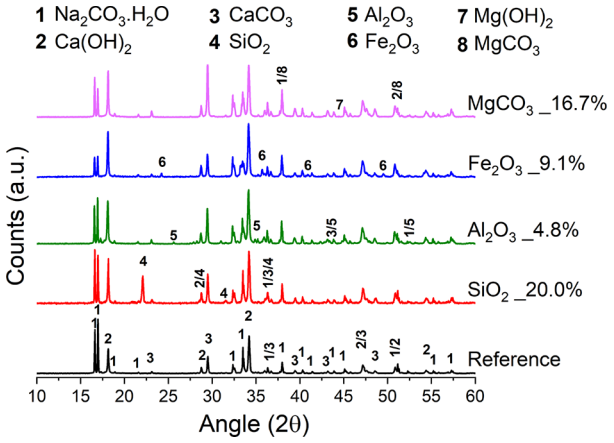

Figure 7. XRD patterns of the reference, SiO_2_20.0%, Al_2O_3_4.8%, Fe_2O_3_9.1%, and $MgCO_3$_16.7% samples with main crystalline phases highlighted.

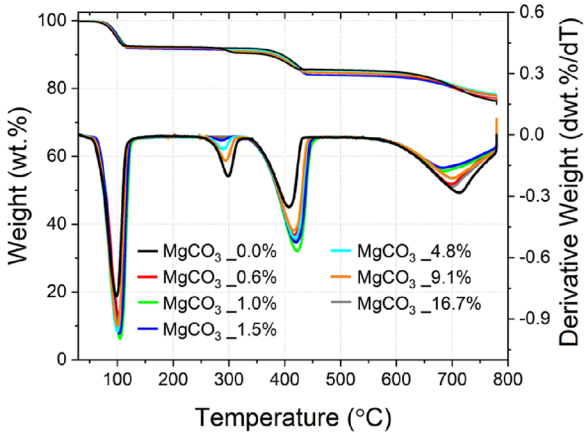

Figure 8. TG and DTG trends observed for the binary system $CaCO_3$:$MgCO_3$ reported in Table 3.

$$Na_{wt\%} = \frac{wt\%_{Na_2CO_3\cdot H_2O}}{MW_{Na_2CO_3\cdot H_2O}} \times 2MW_{Na} \quad (3)$$

$$Ca_{wt\%} = \frac{wt\%_{Ca(OH)_2}}{MW_{Ca(OH)_2}} \times MW_{Ca} + \frac{wt\%_{CaCO_3}}{MW_{CaCO_3}} \times MW_{Ca} \quad (4)$$

The contents of Na and Ca gained from the TG analysis and respective calculations are in good agreement with the XRF data recorded on targeted samples, as reported in Figure 9. A slight overestimation of the Ca-containing species ($CaCO_3$ and $Ca(OH)_2$) was gained from the TG analysis of the samples SiO_2_20% and $MgCO_3$_16.7%, with respect to XRF (Figure 9). Despite that, the theoretical Ca content calculated by considering the $Na_{wt\%}$ in the sample, referring to the product $Na_2CO_3{\cdot}H_2O$, was higher than the value gained from XRF. Potentially, the higher Si and Mg content in the samples SiO_2_20% and $MgCO_3$_16.7%, respectively, could be the

https://doi.org/10.1021/acssuschemeng.2c02913
ACS Sustainable Chem. Eng. 2022, 10, 11913−11925

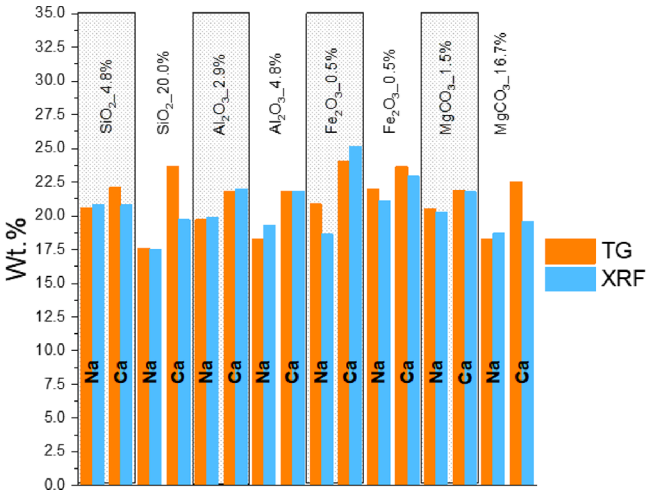

Figure 9. Effect of impurity contents on the amount of Na and Ca in the solid reaction products (data obtained by XRF and TG): the type and quantity of the impurity are indicated at the top.

cause of a slight underestimation of Ca through XRF. However, despite the fact that these values were slightly off, the overall good correspondence between the TG and XRF data was likely suggesting a high reliability of the phase quantification, and linked conversion efficiency α, performed through TG analysis.

Based on the TG data, the amounts of $Na_2CO_3{\cdot}H_2O$, $Ca(OH)_2$, and $CaCO_3$ were calculated for each solid reaction product to estimate the extent of decarbonization reaction as shown in Figure 10.

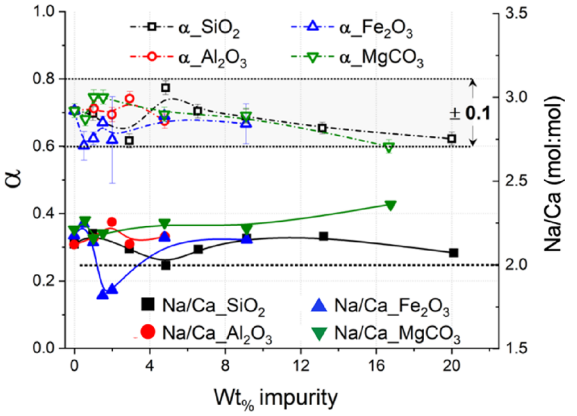

Figure 10. Conversion extent (α) and Na/Ca (mol %/mol %) ratios, calculated through eqs 5 and 6, for all the binary systems shown here. The lines only work as a guide for the eye.

Moreover, to gain a better understanding of the precipitation of the main products $Ca(OH)_2$ and $Na_2CO_3{\cdot}H_2O$ or Na_2CO_3, $Na_{mol\ \%}$ and $Ca_{mol\ \%}$ were first expressed in eqs 5 and 6, respectively.

$$Na_{mol\%} = \frac{Na_{wt\%}}{MW_{Na}} \times 100 \quad (5)$$

$$Ca_{mol\%} = 100 \times \frac{wt\%_{Ca(OH)_2}}{MW_{Ca(OH)_2}} \times \frac{MW_{Ca}}{MW_{Ca(OH)_2}} \quad (6)$$

While $Na_{mol\ \%}$ is linearly linked to eq 3 by the molecular weight of Na (MW_{Na}), the $Ca_{mol\ \%}$ here only refers to the fraction of Ca present in the system as $Ca(OH)_2$. By considering these values, it was possible to highlight a Na/Ca molar ratio slightly above 2 for all the samples discussed (Figure 10), apart from the specimens Fe_2O_3_1.5% and Fe_2O_3_2.0%. Since the stoichiometric ratio of the reaction products $Ca(OH)_2$ and $Na_2CO_3{\cdot}H_2O$ or Na_2CO_3 is 1 (eq 1), the Na/Ca molar ratio should be 2. The slightly exceeding values might indicate higher kinetics for the precipitation of $Na_2CO_3{\cdot}H_2O$ or Na_2CO_3 with respect to $Ca(OH)_2$. Another possibility might relate to a partial loss of $Ca(OH)_2$ upon dissolution, leading to higher Na/Ca molar ratios, but this is unlikely since the solubility of $Ca(OH)_2$ is about 220 and 205 times lower than those of $Na_2CO_3{\cdot}H_2O$ and Na_2CO_3, respectively (Table S1).

The efficiency of the reaction varies with the type and amount of the impurity but generally remains at around α = 0.71 with possibly a slight decrease when the amount of impurity increases over 10 wt %. Specifically, increasing contents of Al_2O_3 and $MgCO_3$ were not significantly affecting the reaction efficiency, which remained constant throughout the ranges investigated.

The reactions of the systems with SiO_2 and Fe_2O_3 were prepared twice to experimentally confirm the nonlinear trends detected, and thus, their data in Figure 10 indicate the standard deviation. The efficiency of the reaction appears to slightly increase at 4.8 wt % SiO_2 content. Such a silica content may increase the efficiency of the decarbonization, but additional investigation is required to confirm and elucidate the trend. With Fe_2O_3 impurity, the decarbonization reaction appeared to be reduced at 0.5 and 2.0 wt %, but that might be due to the significant experimental error (Figure 10).

Based on the initial composition and the XRF data of the reaction products, $Si_{wt\ \%}/Ca_{wt\ \%}$, $Al_{wt\ \%}/Ca_{wt\ \%}$, $Fe_{wt\ \%}/Ca_{wt\ \%}$, and $Mg_{wt\ \%}/Ca_{wt\ \%}$ ratios were calculated for the selected systems, as shown in Figure 11. The mass balances prior to and

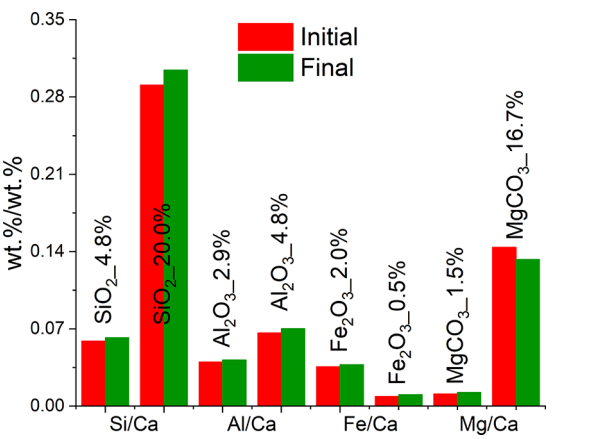

Figure 11. Change in Si/Ca, Al/Ca, Fe/Ca, and Mg/Ca weight ratios between the initial solid mixtures and the solid reaction products.

upon the reaction are not indicating substantial variations for the elements considered, suggesting that the dissolution of those foreign species was not significantly occurring. Such an observation was contradicting the results obtained from the industrial grade chalk and limestone, since silica appeared to dissolve at some extent in those systems (Table 6). Apparently, the reagent grade silica was less reactive than the one within the industrial grade materials, and the reason might be linked

https://doi.org/10.1021/acssuschemeng.2c02913
ACS Sustainable Chem. Eng. 2022, 10, 11913−11925

to the more irregular surface of the latter (Figure S2). The slight overestimation of Mg and Fe for the samples $MgCO_3$_1.5% and Fe_2O_3_0.5%, respectively (Figure 11), could possibly be linked to the low Mg and Fe contents and, therefore, the instrumental error.

The obtained results show that the individual effects of the main impurities of the chalk and limestone tested in the present work are likely minimal on the decarbonization reaction. The relatively short residence time did not allow for the dissolution of SiO_2, Al_2O_3, and Fe_2O_3 in the experiments conducted, except the reaction of $MgCO_3$ to form $Mg(OH)_2$. These phases remain with the solid reaction products upon washing with methanol (Table S1). In terms of application, for instance, for the cement production, the presence of SiO_2, Al_2O_3, Fe_2O_3, and brucite would not represent a problem, as these are the same "impurities" in raw materials used for traditional cement production. Indeed, the presence of silicates and aluminates is crucial for the synthesis of clinker phases.[1]

3.4. Effect of Impurities: Combined Effects. To investigate the combined effect of the impurities, samples were prepared by blending reagent grade materials to simulate the oxide compositions detected for the chalk and limestone (Table 1). Only the main impurity constituents (>1 wt %) detected in the industrial grade materials, such as SiO_2, Al_2O_3, Fe_2O_3, and $MgCO_3$, were considered and blended with reagent grade $CaCO_3$. The compositions of the reagent grade systems considered are reported in Table 4. These mixtures were tested at increasing H_2O/solids ratios, corresponding to decreasing NaOH molarity, as shown in Table 5; the TG/DTG analysis performed on the reaction products is provided in Figure 12A,B.

Similar to the previous experimental results, the recovered solid reaction products indicated weight loss events attributed to the presence of $Na_2CO_3{\cdot}H_2O$ (50−130 °C), $Ca(OH)_2$ (310−470 °C), and $CaCO_3$ (560−800 °C). Both systems indicated a minor formation of monohydrocalcite, reflected by weak weight losses in the region of 150−200 °C for the samples reacted at a water-to-solid ratio of 0.7 (Figure 12A,B). A small weight loss observed in the region of 250−350 °C is likely referred to the dehydration of brucite; more intense signals were detected for L_R.G. with respect to C_R.G., in line with the higher initial $MgCO_3$ content (Table 4).

Based on the amount of $Ca(OH)_2$ and $CaCO_3$ estimated from the TG data, the extent of decarbonization reaction is assessed and indicated in Figure 13.

As reported, the decarbonization for the C_R.G. solids was significantly lower than that for L_R.G. for all the NaOH molarities tested. Although the effects of individual impurities are not clearly identified in the former section, it appears that the efficiency of decarbonization reaction becomes less when the amount of the impurity is larger, as the C_R.G. system has a larger proportion of the total impurity. This suggests either the potential synergetic effect of the impurities or the effect of the NaOH solution used (as NaOH/$CaCO_3$ was set to be 3.0 for all reactions, the C_R.G. system used less NaOH than the same weight of the L_R.G. system). These results are also in contrast with those obtained from the industrial grade calcareous materials (Figure 6), suggesting that the morphology of the materials has a significant impact on the decarbonization reaction in the condition investigated in the present work.

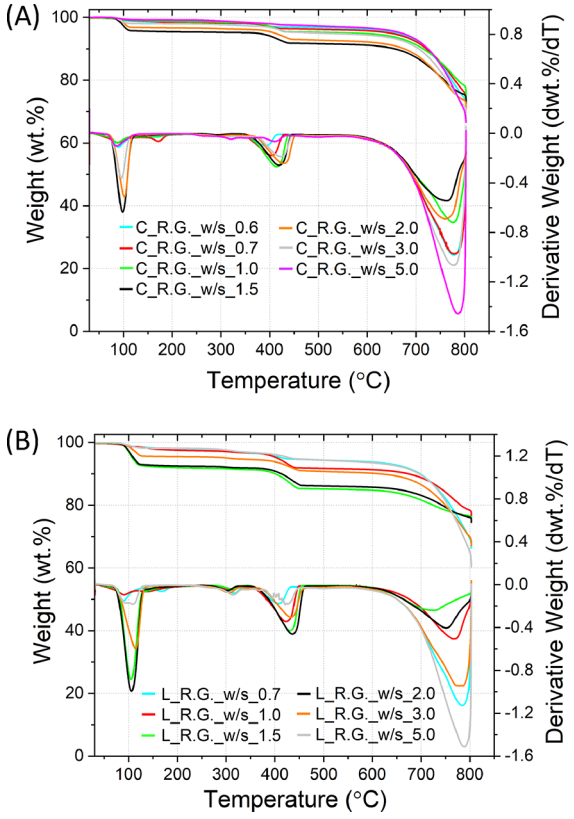

Figure 12. TG and DTG trends observed for the C_R.G._w/s_n (A) and L_R.G._w/s_n (B) samples.

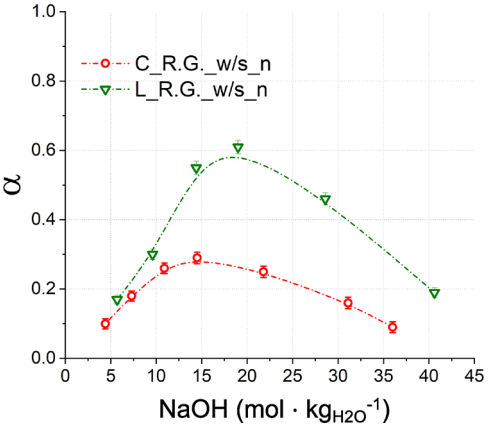

Figure 13. Overview of the conversion extent α registered for the C_R.G. and L_R.G. samples at increasing NaOH molarities.

XRF analysis was also conducted on the samples showing the highest efficiency of decarbonization, i.e., C_R.G._w/s_1.5 (20.0 M NaOH) and L_R.G._w/s_1.5 (15.0 M NaOH). As reported in Figure 14, the proportion of the impurity components in the reaction products remains constant upon the reaction when assuming that the dissolution of $CaCO_3$ and $Ca(OH)_2$ is negligible in the alkaline solutions at the residence times considered here.[49] In other words, the XRF data suggest that the impurities are not likely dissolving in the alkaline solution upon the reaction.

3.5. Discussion. In the decarbonization reaction proposed, the formation of $Ca(OH)_2$ and $Na_2CO_3{\cdot}H_2O$/Na_2CO_3 should theoretically be 1:1 in moles (eq 1); that would theoretically correspond to a Na/Ca molar ratio of 2, with Ca only referring

https://doi.org/10.1021/acssuschemeng.2c02913
ACS Sustainable Chem. Eng. 2022, 10, 11913−11925

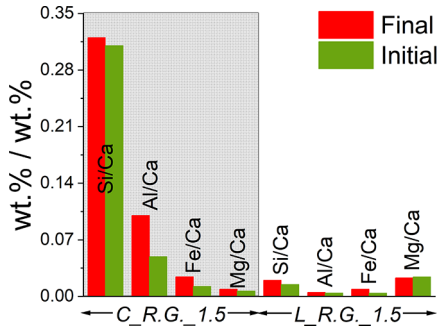

Figure 14. Mass balances for Ca, Si, Al, and Mg expressed as wt % Si/Ca, Al/Ca, Fe/Ca, and Mg/Ca ratios, respectively.

to $Ca(OH)_2$. However, slightly more enhanced precipitation of $Na_2CO_3{\cdot}xH_2O$ was observed with respect to $Ca(OH)_2$ when the effect of $MgCO_3$ was investigated (Figure 10). That might be explained by considering the fact that the surface of calcite is statistically 27% denser in positively charged (Ca^{2+}) sites than negatively charged (CO_3^{2-}) ones,[50] resulting in an enhanced tendency to interact with cationic species, such as Na^+. Accordingly, a higher affinity should be present for Na^+ than OH^- in the system investigated, which may have resulted in the slightly more enhanced precipitation of $Na_2CO_3{\cdot}xH_2O$ than $Ca(OH)_2$. The introduction of $MgCO_3$ would likely provide additional negative binding sites (CO_3^{2-}) interacting with Na^+, leading to a more enhanced precipitation of $Na_2CO_3{\cdot}xH_2O$ than $Ca(OH)_2$.

Decarbonization of industrial grade calcareous materials indicated the higher decarbonization efficiency in the chalk compared with the limestone. This could be likely explained by the higher surface area registered for the chalk, providing a larger number of CO_3^{2-} and Ca^{2+} binding sites for the interaction with Na^+ and OH^- ionic species in the liquid bulk.

Additionally, the larger content of silica within the chalk (Table 1) might potentially play a significant role in terms of reactivity, since it would provide additional Si^{4+} and O^{2-} sites that could interact with the ions in the liquid bulk. However, a lower efficiency in decarbonizing $CaCO_3$ was generally registered for the reagent grade mixture simulating the chalk (Table 4), as reported in Figure 13, suggesting that higher contents of impurities would hinder the reaction at parity of the calcareous source used.

The bell-shaped profile was obtained in the decarbonization efficiency with different NaOH concentrations, both with industrial grade and reagent grade calcareous materials (Figures 6 and 13). To understand the reduced decarbonization efficiency observed at relatively low and high NaOH molarities, it is useful to consider the situation at the solid–liquid interface. In solution, the surface binding sites of the solids are readily saturated with strongly adsorbed layers of water[51] up to four layers below the surface, as shown in Figure 15A. Moreover, it is well known that a diffuse double layer would form at the interface of the solid and liquid bulk upon incorporation within the solid of a charged species.[52] The double layer is electrically charged positively and negatively when adsorbed CO_3^{2-} and Na^+ are considered, respectively, to ensure the electroneutrality of the surface. Apart from the steric encumbrance linked to the layers of water attached to the surface of calcite, this layer would also contribute to the overall energetic barrier to overcome for the uptake of Na^+ and CO_3^{2-} to occur. With a low NaOH concentration, the

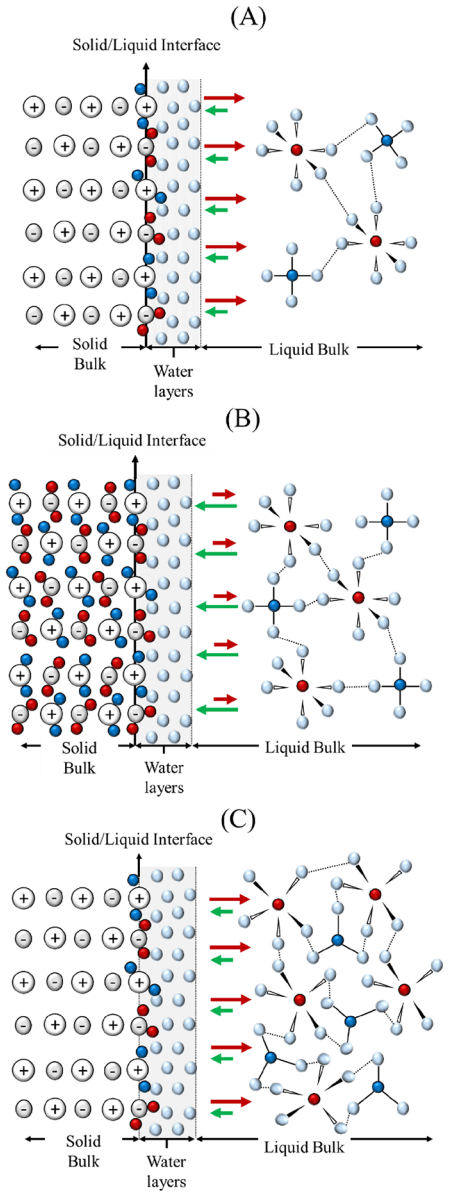

Figure 15. Schematic representation of the interactions occurring within the liquid and solid bulk considered for the study, where the red, dark blue, and light blue colors refer to Na^+, OH^-, and H_2O, respectively. Each Na^+ and OH^- ion is surrounded by a number of water molecules, forming the solvation shell, depending on the NaOH concentration.[53] The hydrogen bonds between the Na^+ and OH^- ions and the water molecules forming the solvation shell and between water molecules of adjacent ions are also displayed. The solid/liquid interface is highlighted in light gray, outlining the attachment of those four layers of water, whereas the green and red arrows qualitatively represent the attractive and repulsive forces between the ions in solution and the solid surface. Cases A, B, and C refer to low, medium/optimal, and high NaOH concentrations, respectively.

chemical potential in the liquid bulk would not be sufficient to overcome the energetic barrier for the nucleation and precipitation to occur. However, the limited reaction efficiencies suggest that the low NaOH concentration was enough to at least saturate the surface binding sites of the solid calcite beneath the layer of water as indicated in Figure 15A. When the NaOH concentration increases, as shown in Figure 15B, its chemical potential in the liquid bulk becomes sufficient both for the saturation of the surface binding sites and for

https://doi.org/10.1021/acssuschemeng.2c02913
ACS Sustainable Chem. Eng. 2022, 10, 11913−11925

promoting the nucleation and precipitation, diffusing toward the inner part of the solids. However, when the NaOH concentrations become too high, as shown in Figure 15C, the nucleation and precipitation of the reaction product become harder, likely given the too high activity of the ions. Moreover, the higher viscosity of the NaOH solution might have lowered the contact with the solid reactants.

Figure 15

4. CONCLUSIONS

An alternative no-combustion $CaCO_3$ decarbonization route, involving the production of $Ca(OH)_2$ and direct capture of the process CO_2 into $Na_2CO_3{\cdot}xH_2O$, on industrial grade calcareous materials was investigated. The reaction efficiency was higher for a type of chalk rich in SiO_2 (19.9 wt %) compared with limestone mostly composed of $CaCO_3$ (94.4 wt %). The maximum decarbonization efficiency α of 0.79 was achieved for the chalk reacting with 31.1 M NaOH, while a value of 0.49 was obtained for the limestone with 14.3 M NaOH. The higher irregularity of the chalk surface, likely leading to a larger number of readily available binding sites, is believed to be the main reason behind this efficiency difference. In fact, additional experiments performed with reagent grade reactants highlighted that the solid solution simulating the limestone (rich in $CaCO_3$) was more reactive if the same calcareous source was considered.

The bell-shaped trend observed in the decarbonization efficiency with increasing NaOH molarities was also discussed. Likely, low NaOH concentrations would allow only for the saturation of the surface binding sites of calcite, while the subsequent nucleation and precipitation would be increased at higher concentrations (a higher chemical potential) of NaOH within the liquid. However, the lower conversion efficiency observed at too high NaOH molarities was likely linked to the enhanced viscosity of the liquid bulk, hindering the ionic mobility and further interaction with the solid reactants.

The effect of the major impurities was assessed individually with reagent grade materials, and only slight fluctuations in the reaction efficiency were observed at increasing contents of SiO_2, Al_2O_3, Fe_2O_3, and $MgCO_3$. The elemental analysis of the powders prior to and upon the reaction suggested negligible dissolution of SiO_2, Al_2O_3, and Fe_2O_3, while $MgCO_3$ reacts to form brucite $Mg(OH)_2$.

In conclusion, the present study demonstrated the feasibility of the chemical $CaCO_3$ decarbonization route on different industrial sources without combustion. The effect of microscopic morphology and surface of the $CaCO_3$ source was more significant than that of impurities. This unconventional route for the decarbonization of limestone could minimize the CO_2 emissions both from the conventional calcination of $CaCO_3$ and combustion of fuels, simultaneously sequestrating CO_2 in a stable carbonate mineral form. It has a great potential, with further understanding and development, toward a sustainable future of relevant industries.

ASSOCIATED CONTENT

Supporting Information

The Supporting Information is available free of charge at https://pubs.acs.org/doi/10.1021/acssuschemeng.2c02913.

Table S1: solubility ($g{\cdot}L^{-1}$) of the relevant solid phases in water and methanol at 25 °C and 1 atm; Figure S1: particle size distribution (PSD) performed for both the limestone and chalk studied; Figure S2: SEM micrographs of the silica crystals within the chalk and limestone, together with the reagent grade silica; Figure S3: TG/DTG trends observed for the binary systems $CaCO_3$:SiO_2, Al_2O_3:SiO_2, and Fe_2O_3:SiO_2, reported in Table 4 (PDF)

AUTHOR INFORMATION

Corresponding Authors

Marco Simoni − *Department of Materials Science & Engineering, University of Sheffield, S1 3JD Sheffield, United Kingdom;* orcid.org/0000-0001-5248-851X; Email: marco.simoni.w@gmail.com

Theodore Hanein − *Department of Materials Science & Engineering, University of Sheffield, S1 3JD Sheffield, United Kingdom;* orcid.org/0000-0002-3009-703X; Email: t.hanein@sheffield.ac.uk

Hajime Kinoshita − *Department of Materials Science & Engineering, University of Sheffield, S1 3JD Sheffield, United Kingdom;* Email: h.kinoshita@sheffield.ac.uk

Authors

Chun Long Woo − *Department of Materials Science & Engineering, University of Sheffield, S1 3JD Sheffield, United Kingdom*

John Provis − *Department of Materials Science & Engineering, University of Sheffield, S1 3JD Sheffield, United Kingdom;* orcid.org/0000-0003-3372-8922

Complete contact information is available at: https://pubs.acs.org/10.1021/acssuschemeng.2c02913

Notes

The authors declare no competing financial interest.

ACKNOWLEDGMENTS

This work was funded by the Engineering and Physical Science Research Council (EPSRC) under grant ID EP/R025959/1 and CEMEX. This research utilized the HADES/MIDAS facility at the University of Sheffield established with financial support from EPSRC and BEIS under grant EP/T011424/1. The XRF analysis was performed by AMG Analytical Services, Fullerton Road, Rotherham, South Yorkshire S60 1DL, England. For the purpose of open access, the author has applied a Creative Commons Attribution (CC BY) license to any author accepted manuscript version arising. The group would also like to express gratitude to Mark Tyrer for the support and knowledge received.

REFERENCES

(1) Taylor, H. F. W. *Cement chemistry*; Vol. 2. London, 1997: Thomas Telford, ISBN: 0 7277 2592 0, DOI: 10.1680/cc.25929

(2) Schorcht, F.; Kourti, I.; Scalet, B. M.; Roudier, S.; Sancho, L. D. *Best available techniques (BAT) reference document for the production of cement, lime and magnesium oxide. European Commission Joint Research Centre Institute for Prospective Technological Studies* (Report EUR 26129 EN). Luxembourg: Publications Office of the European Union, 2013, ISBN 978−92−79-32944-9

(3) U.S. Department of the Interior, U.S. Geological Survey, *Mineral commodity summaries 2020*; 2019, National Minerals Information Centre, ISBN 978−1−4113-4283-5

(4) Friedlingstein, P.; Jones, M. W.; O'sullivan, M.; Andrew, R. M.; Hauck, J.; Peters, G. P.; Peters, W.; Pongratz, J.; Sitch, S.; Le Quéré, C.; Bakker, D. C. Global carbon budget 2019. *Earth Syst. Sci. Data* **2019**, *11*, 1783−1838.

(5) Schneider, M.; Romer, M.; Tschudin, M.; Bolio, H. Sustainable cement production—present and future. *Cem. Concr. Res.* **2011**, *41*, 642−650. I
(6) Blamey, J.; Anthony, E. J.; Wang, J.; Fennell, P. S. The calcium looping cycle for large-scale CO_2 capture. *Prog. Energy Combust. Sci.* **2010**, *36*, 260−279.
(7) Dowling, A.; O'Dwyer, J.; Adley, C. C. Lime in the limelight. *J. Cleaner Prod.* **2015**, *92*, 13−22.
(8) Gutiérrez, A. S.; Martínez, J. B. C.; Vandecasteele, C. Energy and exergy assessments of a lime shaft kiln. *Appl. Therm. Eng.* **2013**, *51*, 273−280.
(9) Bui, M.; Adjiman, C. S.; Bardow, A.; Anthony, E. J.; Boston, A.; Brown, S.; Fennell, P. S.; Fuss, S.; Galindo, A.; Hackett, L. A.; Hallett, J. P.; Herzog, H. J.; Jackson, G.; Kemper, J.; Krevor, S.; Maitland, G. C.; Matuszewski, M.; Metcalfe, I. S.; Petit, C.; Puxty, G.; Reimer, J.; Reiner, D. M.; Rubin, E. S.; Scott, S. A.; Shah, N.; Smit, B.; Trusler, J. P. M.; Webley, P.; Wilcox, J.; Mac Dowell, N. Carbon capture and storage (CCS): the way forward. *Energy Environ. Sci.* **2018**, *11*, 1062−1176.
(10) Usón, A. A.; López-Sabirón, A. M.; Ferreira, G.; Sastresa, E. L. Uses of alternative fuels and raw materials in the cement industry as sustainable waste management options. *Renewable Sustainable Energy Rev.* **2013**, *23*, 242−260.
(11) Shi, C.; Jiménez, A. F.; Palomo, A. New cements for the 21st century: The pursuit of an alternative to Portland cement. *Cem. Concr. Res.* **2011**, *41*, 750−763.
(12) Simoni, M.; Wilkes, M. D.; Brown, S.; Provis, J. L.; Kinoshita, H.; Hanein, T. Decarbonising the lime industry: State-of-the-art. *Renewable and Sustainable Energy Reviews* **2022**, *168*, 112765.
(13) Plaza, M. G.; Martínez, S.; Rubiera, F. CO_2 capture, use, and storage in the cement industry: State of the art and expectations. *Energies* **2020**, *13*, 5692.
(14) Naranjo, M.; Brownlow, D. T.; Garza, A. CO_2 capture and sequestration in the cement industry. *Energy Procedia* **2011**, *4*, 2716−2723.
(15) Idem, R.; Wilson, M.; Tontiwachwuthikul, P.; Chakma, A.; Veawab, A.; Aroonwilas, A.; Gelowitz, D. Pilot plant studies of the CO_2 capture performance of aqueous MEA and mixed MEA/MDEA solvents at the University of Regina CO_2 capture technology development plant and the boundary dam CO_2 capture demonstration plant. *Ind. Eng. Chem. Res.* **2006**, *45*, 2414−2420.
(16) *Bewahrtes neu denken, Environmental data of the German cement industry 2020*;. Duesseldorf, July, 2021, https://www.vdz-online.de/en/knowledge-base/publications/environmental-data-of-the-german-cement-industry-2020, date of access *16*.08.2022
(17) Busch, P.; Kendall, A.; Murphy, C. W.; Miller, S. A. Literature review on policies to mitigate GHG emissions for cement and concrete. *Resour., Conserv. Recycl.* **2022**, *182*, No. 106278.
(18) Hanein, T.; Simoni, M.; Woo, C. L.; Provis, J. L.; Kinoshita, H. Decarbonisation of calcium carbonate at atmospheric temperatures and pressures, with simultaneous CO_2 capture, through production of sodium carbonate. *Energy Environ. Sci.* **2021**, *14*, 6595−6604.
(19) Lakshmanan, S.; Murugesan, T. The chlor-alkali process: work in progress. *Clean Technol. Environ. Policy* **2014**, *16*, 225−234.
(20) Rhodes, C. J. The 2015 Paris climate change conference: COP21. *Sci. Prog.* **2016**, *99*, 97−104.
(21) Neubauer, J.; Pöllmann, H. Alinite—Chemical composition, solid solution and hydration behaviour. *Cem. Concr. Res.* **1994**, *24*, 1413−1422.
(22) Simoni, M.; Hanein, T.; Duvallet, T. Y.; Jewell, R. B.; Provis, J. L.; Kinoshita, H. Producing cement clinker assemblages in the system: $CaO\text{-}SiO_2\text{-}Al_2O_3\text{-}SO_3\text{-}CaCl_2\text{-}MgO$. *Cem. Concr. Res.* **2021**, *144*, No. 106418.
(23) Ramirez, A.; Sarathy, S. M.; Gascon, J. CO_2 derived E-fuels: research trends, misconceptions, and future directions. *Trends Chem.* **2020**, *2*, 785−795.
(24) Meier, A.; Bonaldi, E.; Cella, G. M.; Lipinski, W.; Wuillemin, D. Solar chemical reactor technology for industrial production of lime. *Sol. Energy* **2006**, *80*, 1355−1362.
(25) Murray, A.; Price, L. *Use of alternative fuels in cement manufacture: analysis of fuel characteristics and feasibility for use in the Chinese cement sector*; 2008, Retrieved from https://escholarship.org/uc/item/8sf9s522
(26) Manzano, H.; Durgun, E.; Abdolhosseine Qomi, M. J.; Ulm, F. J.; Pellenq, R. J.; Grossman, J. C. Impact of chemical impurities on the crystalline cement clinker phases determined by atomistic simulations. *Cryst. Growth Des.* **2011**, *11*, 2964−2972.
(27) Palmer, A. N. Origin and morphology of limestone caves. *Geol. Soc. Am. Bull.* **1991**, *103*, 1−21.
(28) Fabricius, I. L. Chalk: composition, diagenesis and physical properties. *Bull. Geol. Soc. Den.* **2007**, *55*, 97−128. Retrieved from http://2dgf.dk/publikationer/bulletin/index.html
(29) Ehrenberg, S. N.; Eberli, G. P.; Keramati, M.; Moallemi, S. A. Porosity-permeability relationships in interlayered limestone-dolostone reservoirs. *AAPG Bull.* **2006**, *90*, 91−114.
(30) Yang, Y.; Aplin, A. C. A permeability−porosity relationship for mudstones. *Mar. Pet. Geol.* **2010**, *27*, 1692−1697.
(31) Zelić, J.; Rušić, D.; Krstulović, R. Kinetic analysis of thermal decomposition of $Ca(OH)_2$ formed during hydration of commercial Portland cement by DSC. *J. Therm. Anal. Calorim.* **2002**, *67*, 613−622.
(32) Gallagher, P. K.; Johnson, D. W., Jr. The effects of sample size and heating rate on the kinetics of the thermal decomposition of $CaCO_3$. *Thermochim. Acta* **1973**, *6*, 67−83.
(33) Hartman, M.; Trnka, O.; Veselý, V.; Svoboda, K. Thermal dehydration of the sodium carbonate hydrates. *Chem. Eng. Commun.* **2001**, *185*, 1−16.
(34) Kjellsen, K. O.; Monsøy, A.; Isachsen, K.; Detwiler, R. J. Preparation of flat-polished specimens for SEM-backscattered electron imaging and X-ray microanalysis—importance of epoxy impregnation. *Cem. Concr. Res.* **2003**, *33*, 611−616.
(35) Potts, P. J.; Ellis, A. T.; Kregsamer, P.; Streli, C.; Vanhoof, C.; West, M.; Wobrauschek, P. Atomic spectrometry update. X-ray fluorescence spectrometry. *J. Anal. At. Spectrom.* **2005**, *20*, 1124−1154.
(36) Seidell, A. *Solubilities of inorganic and metal organic compounds*; 1940, Van Nostrand.
(37) Farhad, A.; Mohammadi, Z. Calcium hydroxide: a review. *Int. Dent. J.* **2005**, *55*, 293−301.
(38) Ellingboe, J. L.; Runnels, J. H. Solubilities of Sodium Carbonate and Sodium Bicarbonate in Acetone-Water and Methanol-Water Mixtures. *J. Chem. Eng. Data* **1966**, *11*, 323−324.
(39) Morey, G. W. The action of water on calcite, magnesite and dolomite. *Am. Mineral.: J. Earth Planet. Mater.* **1962**, *47*, 1456−1460. ISSN: 0003-004X
(40) Alexander, G. B.; Heston, W. M.; Iler, R. K. The solubility of amorphous silica in water. *J. Phys. Chem.* **1954**, *58*, 453−455.
(41) Patnaik, P. *Handbook of inorganic chemicals*; Vol. *529*. 2003: McGraw-Hill: New York, ISBN: 0−07−049439-8
(42) Young, J. R.; Davis, S. A.; Bown, P. R.; Mann, S. Coccolith ultrastructure and biomineralisation. *J. Struct. Biol.* **1999**, *126*, 195−215.
(43) Cizer, Ö.; Rodriguez-Navarro, C.; Ruiz-Agudo, E.; Elsen, J.; Van Gemert, D.; Van Balen, K. Phase and morphology evolution of calcium carbonate precipitated by carbonation of hydrated lime. *J. Mater. Sci.* **2012**, *47*, 6151−6165.
(44) Cheng, B.; Lei, M.; Yu, J.; Zhao, X. Preparation of monodispersed cubic calcium carbonate particles via precipitation reaction. *Mater. Lett.* **2004**, *58*, 1565−1570.
(45) Simoni, M.; Hanein, T.; Woo, C. L.; Tyrer, M.; Nyberg, M.; Martinez, J. C.; Quintero-Mora, N. I.; Provis, J. L.; Kinoshita, H. Decarbonisation of calcium carbonate in sodium hydroxide solutions under ambient conditions: effect of residence time and mixing rates. *Phys. Chem. Chem. Phys.* **2022**, *24*, 16125−16138.
(46) Ball, M. C.; Taylor, H. F. W. The dehydration of brucite. *Mineral. Mag. J. Mineral. Soc.* **1961**, *32*, 754−766.

(47) Kimura, T.; Koga, N. Thermal dehydration of monohydrocalcite: overall kinetics and physico-geometrical mechanisms. *J. Phys. Chem. A* **2011**, *115*, 10491−10501.
(48) Deshpande, D. A.; Ghormare, K. R.; Jawadekar, V. L.; Deshpande, N. D. Thermal analysis of $Na_2CO_3 \cdot H_2O$ crystals. *Thermochim. Acta* **1983**, *60*, 295−302.
(49) Duchesne, J.; Reardon, E. J. Measurement and prediction of portlandite solubility in alkali solutions. *Cem. Concr. Res.* **1995**, *25*, 1043−1053.
(50) Heberling, F.; Bosbach, D.; Eckhardt, J. D.; Fischer, U.; Glowacky, J.; Haist, M.; Kramar, U.; Loos, S.; Müller, H. S.; Neumann, T.; Pust, C.; Schäfer, T.; Stelling, J.; Ukrainczyk, M.; Vinograd, V.; Vučak, M.; Winkler, B. Reactivity of the calcite−water-interface, from molecular scale processes to geochemical engineering. *Appl. Geochem.* **2014**, *45*, 158−190.
(51) Stipp, S. L.; Hochella, M. F., Jr. Structure and bonding environments at the calcite surface as observed with X-ray photoelectron spectroscopy (XPS) and low energy electron diffraction (LEED). *Geochim. Cosmochim. Acta* **1991**, *55*, 1723−1736.
(52) Stillinger, F. H., Jr.; Kirkwood, J. G. Theory of the diffuse double layer. *J. Chem. Phys.* **1960**, *33*, 1282−1290.
(53) Botti, A.; Bruni, F.; Imberti, S.; Ricci, M. A.; Soper, A. K. Ions in water: The microscopic structure of concentrated NaOH solutions. *J. Chem. Phys.* **2004**, *120*, 10154−10162.

https://doi.org/10.1021/acssuschemeng.2c02913
ACS Sustainable Chem. Eng. 2022, 10, 11913−11925